ACS Photonics

pubs.acs.org/journal/apchd5

Article

Purcell Enhancement and Wavelength Shift of Emitted Light by $CsPbI_3$ Perovskite Nanocrystals Coupled to Hyperbolic Metamaterials

Hamid Pashaei Adl, Setatira Gorji, Mojtaba Karimi Habil, Isaac Suárez, Vladimir S. Chirvony, Andrés F. Gualdrón-Reyes, Iván Mora-Seró, Luisa M. Valencia, María de la Mata, Jesús Hernández-Saz, Sergio I. Molina, Carlos J. Zapata-Rodríguez,* and Juan P. Martínez-Pastor*

Cite This: *ACS Photonics* 2020, 7, 3152−3160

Read Online

ACCESS | Metrics & More | Article Recommendations | Supporting Information

ABSTRACT: Manipulation of the exciton emission rate in nanocrystals of lead halide perovskites (LHPs) was demonstrated by means of coupling of excitons with a hyperbolic metamaterial (HMM) consisting of alternating thin metal (Ag) and dielectric (LiF) layers. Such a coupling is found to induce an increase of the exciton radiative recombination rate by more than a factor of three due to the Purcell effect when the distance between the quantum emitter and HMM is nominally as small as 10 nm, which coincides well with the results of our theoretical analysis. Besides, an effect of the coupling-induced long wavelength shift of the exciton emission spectrum is detected and modeled. These results can be of interest for quantum information applications of single emitters on the basis of perovskite nanocrystals with high photon emission rates.

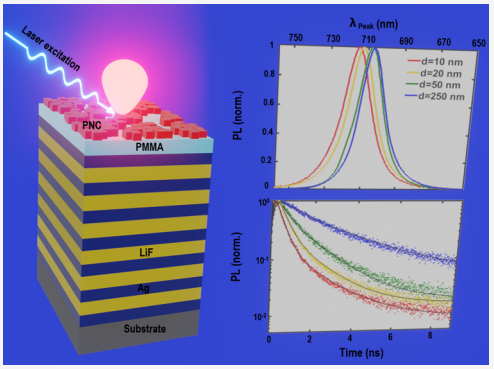

KEYWORDS: *lead halide perovskites, perovskite nanocrystals, photonics, hyperbolic metamaterials (HMMs), light−matter interaction, Purcell factor*

The manipulation of the spontaneous emission rate is indispensable for a wide variety of technological photonic applications ranging from light emitting diodes to single photon sources. From one side, nanofabrication techniques have enabled the development of different optical metamaterials, which are designed to achieve and exploit light−matter interaction unattainable with natural materials.[1−4] Among the varieties of metamaterials proposed and fabricated so far, hyperbolic metamaterials (HMMs)[5−8] have rapidly gained a key role in nanophotonics due to their peculiar ability to manipulate the near field of a quantum emitter (QE).[9−11] The most intriguing feature of these anisotropic HMM structures is the increase of the photon density of states, which can be used to engineer the light−matter interaction, particularly with emitters, by increasing their emission rates when they are placed close to the HMM surface. Moreover, the position of the emitter in the plane (parallel to the HMM surface) is not critical, only its distance to the HMM surface, to obtain a certain Purcell factor, contrary to the case of resonators, where the Purcell factor decreases enormously when the single emitter does not overlap the maximum of the electric field defined in the cavity. Of course, HMMs can be also further engineered and improved by nanostructuration for obtaining greater Purcell factors.[12] On the other hand, the optical and electrical properties of lead halide perovskites (LHPs) have allowed consideration of these promising materials for developing high quality optoelectronic devices under cheap, straightforward, and low temperature technologies.[13−19] Recently, fully inorganic perovskite nanocrystals (PNCs) of cesium lead halides ($CsPbX_3$, X = Cl, Br, I) were synthesized with precise size and compositional control, tunable, narrow-band emission, and high photoluminescence quantum yield (PLQY) over the whole visible wavelength range.[20−25] At the level of single nanocrystals, LHPs can be also potential candidates for single photon sources.[26−31] For quantum information applications, it is important to increase the photon emission rate (or radiative rate) of a QE, which is commonly achieved by embedding single photon nanomaterials into optical microcavities.[32−36] The photon emission rate enhancement has been experimentally investigated using periodical metal-dielectric structures for different types of single emitters (dye molecules, metal−organic complexes, and quantum

Received: August 2, 2020
Published: October 26, 2020

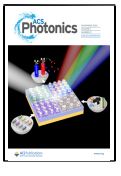

dots),[37−40] as also confirmed theoretically.[41,42] It is worth noting the study of recombination rate enhancement using a film of $CsPbBr_3$ PNCs deposited by spin coating on top of single and double metal−insulator−metal cavities.[43] The advantage of using HMMs along with simple deposition techniques of PNCs does not require any deterministic positioning of the QE, as in the case of 2D photonic cavities.[44] The coupling of light emitters to the HMM structure would induce an increase of the exciton radiative recombination rate (and therefore a reduction of the exciton radiative lifetime) by the Purcell effect,[45] which would gain importance by decreasing the average distance between a QE and the HMM structure. Besides, the short distance between PNCs and the HMM also affects the photon emission frequency, like in the case of a QE placed near partially reflecting surfaces, which is a widespread feature of the dipole-surface interaction and, in simple terms, results from the coupling between the dipole and its own image in the metal surface. However, such a shift of the emitted photon frequency is theoretically expected to be very small,[46−51] hindering its experimental determination.

In the present work, we propose the manipulation of photons produced by exciton radiative recombination in $CsPbI_3$ PNCs by means of HMM structures. They consist of several alternating metal (Ag) and dielectric (LiF) layers, whose thickness and period affect the dielectric constant anisotropy and optical modes. The coupling between $CsPbI_3$ PNCs and the HMM modes is controlled by a variable dielectric spacer thickness (investigated in the range of 10−50 nm). Our analysis in terms of the Purcell factor suggests that the confined optical modes are sustained by near field interactions between the emitters and the HMM structure. However, for achieving a successful exciton-HMM coupling, radiative recombination of excitons is a prerequisite, which is undoubtedly achieved in most semiconductors at cryogenic temperatures. The exciton-HMM coupling in our system will lead to the Purcell-enhanced spontaneous emission by a factor greater than three for the thinnest spacer (10 nm), together with a photoluminescence red shift as high as 8 nm (around 20 meV). On the basis of our literature analysis, no precedent is found for such a noticeable emission frequency shift for PNCs on top of HMM structures. Both experimental observations, the Purcell effect and the emitter frequency shift, have been successfully explained theoretically.

EXPERIMENTAL DETAILS AND METHODS

Synthesis of $CsPbI_3$ Nanocrystals. $CsPbI_3$ PNCs were synthesized following the hot-injection method described by Kovalenko and co-workers,[20] with some modifications.[52] All the reactants were used as received without an additional purification process. Briefly, a Cs-oleate solution was prepared by mixing 0.41 g of Cs_2CO_3 (Sigma-Aldrich, 99.9%), 1.25 mL of oleic acid (OA, Sigma-Aldrich, 90%), and 20 mL of 1-octadecene (1-ODE, Sigma-Aldrich, 90%) which were loaded together into a 50 mL three-neck flask at 120 °C under a vacuum for 1 h under constant stirring. Then, the mixture was N_2-purged and heated at 150 °C to reach the complete dissolution of Cs_2CO_3. The solution was stored under N_2, keeping the temperature at 100 °C to prevent Cs-oleate oxidation. For the synthesis of $CsPbI_3$ PNCs, 1.0 g of PbI_2 (ABCR, 99.999%), and 50 mL of 1-ODE were loaded into a 100 mL three-neck flask. The mixture was simultaneously degassed and heated at 120 °C for 1 h under constant stirring. Then, a mixture of 5 mL each of both pretreated (130 °C) OA and oleylamine (OLA, Sigma-Aldrich, 98%) were separately added to the flask under N_2, and the mixture was quickly heated at 170 °C. Simultaneously, 4 mL of Cs-oleate solution was quickly injected to the mixture, and then, the reaction was quenched to immerse the mixture into an ice bath for 5 s. In order to perform the isolation process of PNCs, the colloidal solutions were centrifugated at 4700 rpm for 10 min. Then, PNCs pellets were separated after discarding the supernatant and redispersed in hexane to concentrate the PNCs at 50 mg/mL.

Methodologies. Metal (Ag) and dielectric (LiF) layers were deposited by thermal evaporation under high vacuum (2×10^{-5} mbar) on top of a silicon wafer, which was preliminary cleaned by following the procedure reported in ref 53. The morphology of fabricated HMM structures was characterized by HAADF-STEM using a FEI TALOS F200X at 200 kV, equipped with a field emission gun (FEG) source, that combines high resolution (S)TEM imaging with energy-dispersive X-ray (EDS) signal detection. Cross-section TEM samples were prepared using a Zeiss Auriga FIB, and the samples were placed on a copper grid. The specular reflectance of the same HMM structures was measured at single wavelengths using different lasers by a homemade set up incorporating a goniometer for the HMM-holder and detector ($\theta-2\theta$ configuration). For low temperature photoluminescence (PL) and time-resolved PL (TRPL) measurements, the samples were held in the coldfinger of a closed-cycle He cryostat (ARS DE-202), which can be cooled down to 15 K, approximately. PL was excited by means of 200 fs pulsed Ti:sapphire passive mode-locked laser (Coherent Mira 900D, 76 MHz repetition rate) operating at a wavelength of 810 nm and doubled to 405 nm by using a BBO crystal. The PL signal was dispersed by a double 0.3 m focal length grating spectrograph (Acton SP-300i from Princeton Instruments) and detected with a cooled Si CCD camera (Newton EMCCD from ANDOR) for PL spectral measurements and with a silicon single photon avalanche photodiode (micro photon device) connected to a time-correlated single-photon counting electronic board (TCC900 from Edinburgh Instruments) for TRPL measurements.

RESULTS AND DISCUSSION

The HMM structure consisted of six periods (eight periods in the case of the structure included in the Supporting Information) of alternating metal (Ag) and dielectric (LiF) layers and finished in the metal (Ag) deposited by thermal evaporation on a silicon wafer, as illustrated in Figure 1a. Two HMM structures were grown with different nominal period and thicknesses of metal and dielectric layers and real thicknesses were estimated at the center of the wafer by HAADF-STEM. Figure 1b shows an HAADF image (Z-contrast) of the HMM evidencing the alternation of Ag (brighter material) and LiF (darker material) layers, whose chemical composition has been further checked by EDS measurements summarized in the right panel of Figure 1b (Ag, F, and Si mapped signals displayed in magenta, cyan and blue, respectively). These analyses allow extracting the thickness of individual layers. Particularly, the average thickness of Ag + LiF layers was around 25 + 35 nm in the HMM structure shown in Figure 1b and 40 + 40 nm in the HMM structure of Figure S1 (see Supporting Information). On the basis of a simple effective medium model for multilayered structures, our

https://dx.doi.org/10.1021/acsphotonics.0c01219
ACS Photonics 2020, 7, 3152−3160

fabricated HMMs would exhibit a hyperbolic permittivity dispersion at $\lambda \geq 370$ nm, with $\epsilon_x = \epsilon_y = \epsilon_\parallel < 0$ and $\epsilon_z = \epsilon_\perp > 0$ (see Figure 1a for axes notations).[54]

$$R = |r|^2 = \begin{cases} \left|\frac{\sin(\theta - \theta_t)}{\sin(\theta + \theta_t)}\right|^2, & \theta_t = \arcsin\left(\frac{\sin\theta}{\sqrt{\epsilon_\parallel}}\right) \quad \text{s-polarization} \\ \left|\frac{\epsilon_\parallel \tan\theta_t - \tan\theta}{\epsilon_\parallel \tan\theta_t + \tan\theta}\right|^2, & \theta_t = \arctan\sqrt{\frac{\epsilon_\perp \sin^2\theta}{\epsilon_\parallel\epsilon_\perp - \epsilon_\parallel \sin^2\theta}} \quad \text{p-polarization} \end{cases} \tag{1}$$

$$\begin{cases} \epsilon_\parallel = \dfrac{(1+f)\epsilon_{Ag}\epsilon_{LiF} + (1-f)\epsilon_{LiF}^2}{(1-f)\epsilon_{Ag} + (1+f)\epsilon_{LiF}} \\ \epsilon_\perp = f\epsilon_{Ag} + (1-f)\epsilon_{LiF} \end{cases} \tag{2}$$

where f is the fill factor or fraction of metal in the unit cell, i.e., $f = \frac{d_{Ag}}{(d_{Ag} + d_{LiF})}$, as determined by metal and dielectric thicknesses d_{Ag} and d_{LiF}, and θ is the incident angle of light. The hyperbolic dispersion of the HMM has been confirmed experimentally, where the values of electric permittivity were inferred from the fits of angular reflectance profiles measured at λ = 785 nm (similar angular reflectance profiles were also measured in the HMM with Ag + LiF layers 40 + 40 nm thick by using other wavelengths, as shown in Figure S2 of the Supporting Information) in s and p polarizations (data symbols in Figure 1c) to the numerically calculated curves by MATLAB using eqs 1 and 2[55] (red and blue continuous lines in Figure 1c). These layered metal-dielectric structures support a large number of electromagnetic states,[56] which is the key point to understand the potential applications of HMMs in future quantum technologies. To confirm these optical modes in our fabricated HMMs is interesting to calculate the local density of states $\rho(r_0, \omega)$ at a frequency ω_0 by means of the well-known dyadic Green's functions:[54]

$$\rho(\vec{r_0}, \omega_0) = \frac{2\omega_0}{\pi c^2} Im\{Tr[\vec{G}(\vec{r_0}, \vec{r_0}; \omega_0)]\} \tag{3}$$

where c is the speed of light. The local density of states (LDOS) of the HMM was calculated using eq 3 and shown in Figure 1d and Figure S1b (Supporting Information) for the different modes of the two fabricated HMM structures, respectively, as a function of $k_\parallel$.

For these HMMs, we expect a Purcell enhancement of the radiative emission rate of $CsPbI_3$ nanocrystals due to their exciton coupling to plasmonic HMM modes. For observation of this effect, similarly to the case of only metal surfaces, we need to introduce a spacer layer of variable thickness d between the HMM structure and the PNCs (Figure 2a). The spacer is made of poly(methyl methacrylate) (PMMA) spin coated on the HMM structure at 3000 rpm. Finally, on top of the PMMA spacer layer, $CsPbI_3$ PNCs were deposited by dip coating the substrate into the colloidal solution (1 mg/mL of PNCs in hexane) during 1 min.

It is worth mentioning that the above concentration and dipping time were optimized to obtain a partially covered monolayer of $CsPbI_3$ nanocubes (with 14 nm of average cube edge),[57] as illustrated in Figure 2a. This single monolayer of PNCs (meaning a layer made of single nanocrystals dispersed throughout the sample surface without agglomeration, nominally) would ensure an efficient coupling of the emitters to the HMM for a given spacer, because the average PNC-HMM coupling strength would decrease significantly for too thick PNC films, as it would occur if increasing the spacer thickness. Four samples were fabricated with nominal spacer thicknesses d = 10, 20, 50, and 250 nm. The thickest one is considered here as a reference because the exciton-HMM coupling is expected to be negligible in this case.

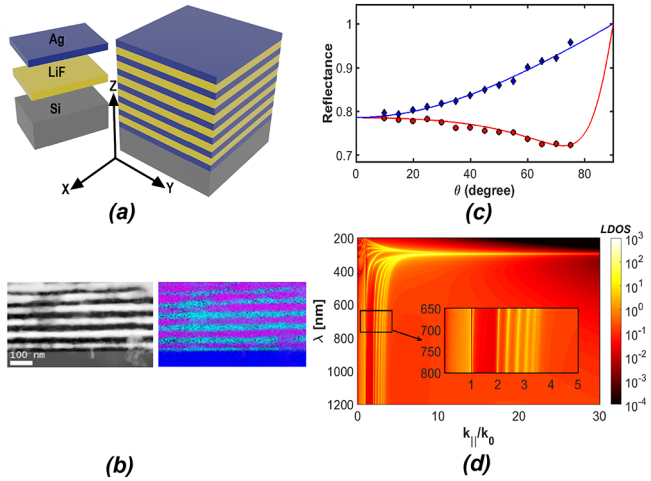

Figure 1. (a) Schematic representation of thermally evaporated HMM structures, (b) HAADF-STEM image and the corresponding EDX map (Ag, F, and Si are displayed in magenta, cyan, and blue, respectively) of a fabricated HMM structure. (c) Angular reflectance spectra of fabricated HMM structures measured at λ = 785 nm and fitted with $\epsilon_\parallel = -4.19 + 1.34i$, $\epsilon_\perp = +1.56 + 0.01i$. Blue diamonds and red circles refer to the s and p polarizations, and solid lines correspond to the simulation. (d) Local density of states (LDOS) computed in the near field of the HMM structure with 10 nm spacer.

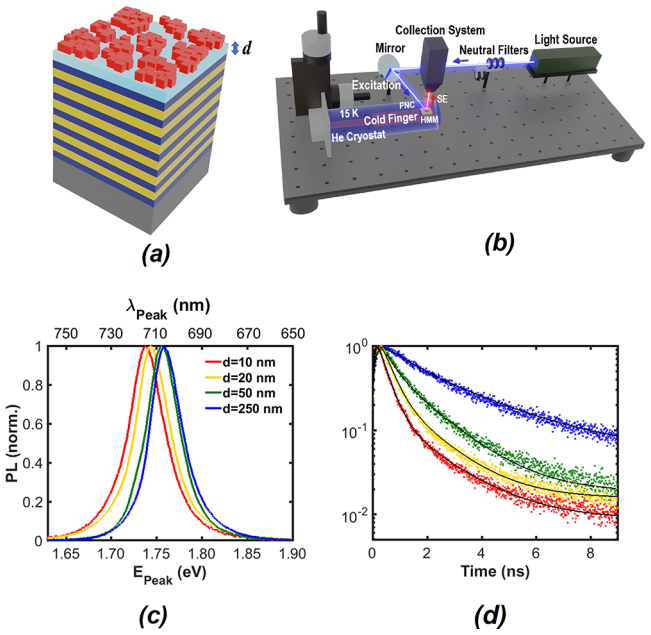

Figure 2. (a) Schematic representation of a HMM structure with a monolayer of PNCs on top of the spacer with thickness d. (b) Schematic illustration of experimental setup for measuring PL and TRPL spectra of PNCs at low temperatures. (c) PL spectra of $CsPbI_3$ PNCs deposited on top of HMM substrates for different spacer thicknesses. (d) PL decay kinetics of $CsPbI_3$ PNCs corresponding to (c).

https://dx.doi.org/10.1021/acsphotonics.0c01219
ACS Photonics 2020, 7, 3152−3160

Figure 2b illustrates the experimental setup for PL and TRPL measurements in backscattering geometry from 15 to 300 K. First of all, it is worth noting that we observe a very weak or meaningless effect of the HMM structure (d = 20 nm) on the PL decay kinetics of $CsPbI_3$ PNCs at room temperature, as shown in Figure S3a of the Supporting Information, whereas at 15 K the same sample demonstrated a clear reduction of the PL decay time (Figure S3b of the Supporting Information). Besides, at room temperature, the PL decay kinetics turn out to be much longer than at 15 K. The origin of the different behavior at room and low temperatures is in the mechanism responsible for the PL decay formation in PNCs. Following the recently proposed concept of delayed luminescence,[58,59] the experimentally observed PL decay kinetics in PNCs are formed with a participation of shallow nonquenching traps, which result in lengthening of the kinetics due to the multiple trapping-detrapping process (a three-level model should be applied in this case[58,59]). In fact, this model could account of the complex PL decay and important changes in PLQY observed at room temperature for $CsPbBr_3$ PNCs in ref 43. This is the reason why one should take with due precaution these previous results using PNCs interacting with metal-dielectric cavities.[43] Since at low temperatures the trapped excitons cannot be longer detrapped to free exciton state, participation of shallow traps in formation of the PL decay kinetics is eliminated, and the PL decay is mainly due to the competition of radiative and nonradiative deactivation channels (the two-level model is applicable). Taking into account that nonradiative exciton recombination is negligible for our PNCs at 15 K, the PL decay kinetics is completely described by the exciton radiative recombination rate. A more detailed description of the delayed luminescence model can be found in section 2 of the Supporting Information.

Therefore, we have developed the experiments at cryogenic temperatures with the goal to reduce the influence of carrier trapping/detrapping and exciton nonradiative recombination channels on the Purcell enhancement by the HMM structure (see the observed increase of the Purcell factor by decreasing temperature in Figure S4e,f of the Supporting Information). That is, the radiative recombination of excitons in $CsPbI_3$ PNCs is the main mechanism responsible of the PL decay kinetics measured at 15 K (Figure 2c). In Figure 2c, we have shown normalized PL spectra to highlight the outstanding PL redshift by reducing the spacer thickness, but absolute PL spectra are presented in Figure S5 of the Supporting Information. As shown in this figure, the PL intensity typically decreases when reducing the spacer thickness, which was observed experimentally by other authors and attributed to the preferential emission of light into the high-k metamaterial modes,[60,61] as first explained for the case of a metal surface[62] (surface plasmon modes in this case). In turn, the preferential emission into the high-k modes of the HMM is the origin of the exciton-HMM coupling that gives rise to these remarkable effects (Purcell effect, PL redshift, and decrease of the PL intensity by reducing d).

The PL peak wavelength for the reference sample is observed at around 705 nm, in good agreement with what is reported by other authors for films of $CsPbI_3$ PNCs at cryogenic temperatures.[57,63] We also tested $CsPbBr_3$ PNCs deposited on top of the same HMM, whose spontaneous emission is peaked at around 520 nm. For these emitters, we did not observed any decay time reduction from 300 down to 15 K. This effect is ascribed to the wavelength dependence of the Purcell factor as a function of the metal fill factor in the HMM, which is equal/smaller than 0.5 in our case and consequently exhibiting a negligible Purcell factor enhancement at around 500 nm (see refs 39 and 64 for example, and section 4 of the Supporting Information). In fact, metal fill factors in the HMM close to the unit would give rise to large Purcell factor values as compared to medium-low metal fill factors, but extended in a broader wavelength/energy region in the latter case. On the contrary, the behavior of the HMM in the first case is more similar to that observed for a metal surface. More interestingly, in the samples with a spacer thinner than 50 nm, a clear redshift is observed with a spacer thickness decrease, being up to 8 nm (20 meV) for the case of the sample with the thinnest spacer layer, d = 10 nm. Although this is not an intuitive effect and cannot be easily explained, we unambiguously attribute it to the coupling of perovskite emitters to the HMM modes, as will be discussed below. Simultaneously, we observe a shortening of the measured PL transients by reducing the HMM-spacer thickness (green, yellow and red dotted transients in Figure 2d), as compared to the one measured for the reference sample (blue dotted transient in Figure 2d). As a consequence, the exciton lifetime deduced from PL transients decreases with reducing the spacer, which is ascribed to a change in the electromagnetic radiation distribution in vacuum,[65] i.e., a Purcell factor enhancement, that arises from the optical coupling of the $CsPbI_3$ PNC emitters to the modes of the HMMs. Indeed, a similar Purcell effect was observed in the second HMM structure fabricated with slightly different parameters (40 + 40 nm period), as observed in Figure S3b of the Supporting Information. Therefore, our results are consistent and reproducible, and they are not sample dependent (i.e., not dependent on the quality of the film made of PNCs). Furthermore, the accuracy of the experiments is guaranteed by preparing all samples under similar conditions and measured using the same protocols, the same day after preparation. TRPL spectra recorded at 15 K for all samples were fitted by using a biexponential decay function where the shortest component (of the order of 1 ns) is attributed to the exciton radiative lifetime, whereas the slower component (several ns) demonstrating much lower relative amplitude (at cryogenic temperatures) can be explained by the exciton recombination dynamics involving shallow traps, as briefly introduced above and presented in more detail within section 2 of the Supporting Information. From these TRPL measurements and fittings, we observe a significant reduction of the average exciton radiative lifetime from ∼1.5 ns down to ∼0.5 ns when reducing the PMMA spacer thickness from 250 to 10 nm. The radiative exciton lifetime of 1.5 ns extracted from the reference sample is very close to the values measured in freshly prepared samples on glass substrates and values reported by us and other authors elsewhere.[59,66] As aforementioned, a clear shortening of the exciton radiative recombination time from 1.5 to 0.5 ns was obtained in average, meaning a clear Purcell enhancement around 3 for the thinnest spacer in the HMM-spacer-PNC structure. This value is similar to other cases reported in the literature using similar HMM structures: Sun et al.[67] reported theoretically 3.21 for vertical component of the Purcell factor at d = 50 nm (for random orientation of the radiant dipole this value would be only 1.42); Shalaginov et al.[68] reported experimentally 2.57 for the Purcell factor of nitrogen-vacancy centers at d = 30 nm; Tumkur et al.[69]

https://dx.doi.org/10.1021/acsphotonics.0c01219
ACS Photonics 2020, 7, 3152−3160

reported 1.5−1.4 for a Purcell factor of dye molecules at d = 45 nm, and Jacob et al.[70] reported 1.7 and 1.8 first value comes from calculations and second from measurements when the thickness of the spacer was d = 21 nm.

For the sake of reproducibility and statistics significance of the results, we recorded around 10 PL and TRPL spectra (see Figure S6 of Supporting Information) in the four fabricated HMM-spacer-PNC structures at different excitation points throughout the sample surface. Of course, we observe some dispersion in these curves from point to point, as one would expect statistically. The most striking and surprising finding when analyzing these collections of PL and TRPL data taken at different excitation points for every sample is the observed clear experimental correlation between the PL peak redshift (with respect to the average PL peak measured in the reference sample) and the Purcell factor (ratio $\tau_x(\mathrm{ref})/\tau_x(d)$, where $\tau_x(\mathrm{ref})$ is the average exciton lifetime measured for PNCs on top of the reference HMM sample with d = 250 nm, and $\tau_x(d)$ is the lifetime measured in the other three PNCs-HMM samples with nominal spacers d = 10, 20, and 50 nm) measured at different points of the samples, as observed in Figure 3a. These data evidence two important facts: (i) the

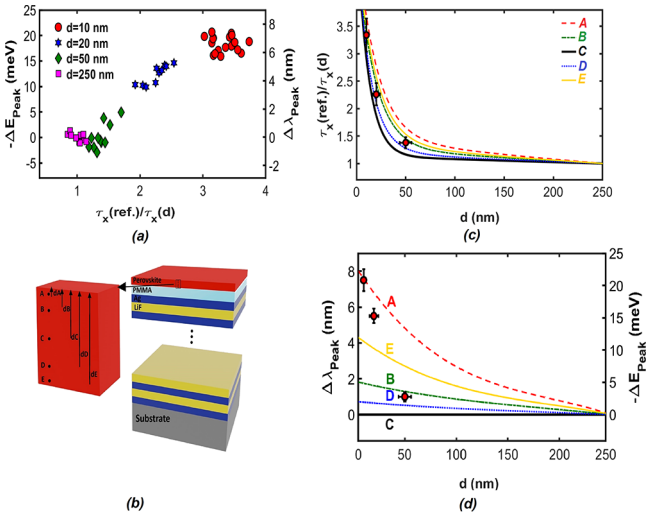

Figure 3. (a) Correlation of the spectral shift and Purcell factor of emitters for the different samples, (b) illustration of a simple model considering a perovskite monolayer on top of PMMA spacer, (c, d) dependence of the Purcell factor and spectral shift as a function of the distance from dipole inside the $CsPbI_3$ and topmost metal surface of the HMM, respectively. Symbols and continuous lines (dashed and dotted-dashed for points A and B, and dotted and solid line for D, E, respectively) correspond to experimental data and simulation, respectively, as described in the text.

data dispersion is more important in samples with thinner spacers (10 and 20 nm) and (ii) even at these data dispersion conditions, we observe a clear correlation between both parameters, the PL peak redshift and Purcell factor. The above mentioned data dispersion is mainly indicative of a certain degree of inhomogeneity in the spacer film thickness. Eventually, even if we optimized the dipping time to cover the HMM + spacer substrate with a single monolayer of PNCs, a certain probability of nanocrystal agglomeration (as also differences in the spin-coated PMMA thickness) is not excluded that would increase the effective value of d. In any case, we can say that a Purcell factor and associated PL peak redshift as high as 3.8 and 8 nm (near 20 meV), respectively, can be measured in some points of the sample with nominal spacer d = 10 nm. In the sample with d = 250 nm (reference), we clearly do not observe changes in the PL peak position, and we only obtain a reasonable dispersion of the exciton lifetime within the range of a 10−15% variation. Both the observed increase in the Purcell factor and the PL peak redshift of PNCs by reducing the spacer thickness should be attributed to the exciton coupling to the HMM modes. In order to explain the experimental results, we propose to consider the model schematically represented in Figure 3b, assuming a monolayer of $CsPbI_3$ PNCs on top of the spacer. In the numerical calculations, the thickness of the $CsPbI_3$ layer and its refractive index are extracted from ref 57 (we are using the same PNCs) and ref 71 respectively. The permittivity of Lithium fluoride (LiF) is taken to be ϵ_{LiF} = 1.95, whereas those of silver (Ag) and silicon (Si) are taken out from refs 72 and 73 respectively.

Once we have obtained the LDOS as explained above (Figure 1d), we can undertake the more complex calculation of the normalized rate of power emission of a radiating dipole which is located at different positions above the spacer layer, as explained below. From here on, we follow the theoretical treatment given in 74 which allows us to write the current density as

$$\vec{j}(\vec{r}) = -i\omega\vec{\mu}\,\delta(\vec{r} - \vec{r_0}) \tag{4}$$

Equation 4 originates from its time derivative, $\vec{j}(\vec{r},t) = \frac{\mathrm{d}}{\mathrm{d}t}\vec{\mu}(t)\delta(\vec{r} - \vec{r_0})$, where $\vec{j}(\vec{r},t) = Re\{\vec{j}(\vec{r})\exp(-i\omega t)\}$ and the dipole moment is $\vec{\mu}(t) = Re\{\vec{\mu}\exp(-i\omega t)\}$; thus, the current density can be thought as an oscillating dipole with origin at the center of the charge distribution. On the other hand, the electric field of an arbitrarily oriented electric dipole located at $\vec{r} = \vec{r}_0$ can be determined by the Green's function $\vec{G}(\vec{r},\vec{r}_0)$:

$$\vec{E}(\vec{r}) = \omega^2\mu\mu_0\vec{G}(\vec{r}, \vec{r_0})\vec{\mu} \tag{5}$$

Finally, after computing the electric field, the normalized rate of power emission reads as[74]

$$\frac{P}{P_0} = 1 + \frac{6\pi\epsilon_0\epsilon}{|\vec{\mu}|^2}\frac{1}{k^3}Im\{\vec{\mu}^*\cdot\vec{E_s}(\vec{r_0})\} \tag{6}$$

where $\vec{E}(\vec{r_0}) = \vec{E_0}(\vec{r_0}) + \vec{E_s}(\vec{r_0})$ and $\vec{E_0}$, $\vec{E_s}$ are the primary dipole and scattered electric fields, respectively. Radiant dipoles would be randomly oriented in nature in the case of cubic nanocrystals used in the present work; thus, a more appropriate estimation for the energy dissipation rate is an average over horizontal and vertical dipoles:

$$\left[\frac{P}{P_0}\right]_{ave} = \frac{1}{3}\left\{\left[\frac{P}{P_0}\right]_{\perp} + 2\left[\frac{P}{P_0}\right]_{\parallel}\right\} \tag{7}$$

The classical enhancement in the radiative emission rate ($P = 1/\tau_x(d)$) with respect to reference ($P_0 = 1/\tau_x(\mathrm{ref})$) will be defined as $\tau_x(d)/\tau_x(\mathrm{ref}) = (P/P_0)^{-1}$. Furthermore, as described above, one of the most important experimental results in the HMM-emitter system is the spectral red shift of the PL peak of emitters. For analytical calculations of this frequency shift of the emitters, again Dyadic Green's function has been used:[74]

$$\frac{\Delta\omega}{\gamma_0} = \frac{6\pi\epsilon_0\epsilon}{|\vec{\mu}|^2}\frac{1}{k^3}Re\{\vec{\mu}^*\cdot\vec{E_s}\} \tag{8}$$

https://dx.doi.org/10.1021/acsphotonics.0c01219
ACS Photonics 2020, 7, 3152−3160

where $\gamma_0 \equiv 1/\tau_x(\text{ref})$, $\tau_x(\text{ref}) = 1.5$ ns. Numerically computed Purcell factor and spectral shift of the emitters with above given equations have been presented respectively in Figure 3c,d as a function of the spacer thickness (continuous lines). Given that the PNC film consists of isolated nanocrystals instead of a continuous perovskite layer, but spatially separated PNCs in the plane (several to hundreds of nm) of slightly different size due to size dispersion introduced by the chemical synthesis (11−16 nm[57]), we have calculated the Purcell factor and PL peak shift of the PNCs by changing the location of the point dipole source inside the continuous perovskite monolayer: curves labeled as A, B, C, D, and E in Figure 3c,d, in correspondence to locations A, B, C, D, and E in Figure 3b, in which points E and D are symmetrical to points A and B with respect to the center, respectively.

The experimental average values for these two magnitudes, from data in Figure 3a, are given by symbols with error bars in Figures 3c,d. As clearly demonstrated by calculated curves in Figure 3d, the PL peak redshift is very sensitive to the location of the point dipole source inside the PNC monolayer. This sensitivity above the center of the $CsPbI_3$ layer (points A−B) is different from below (points D−E) due to the different contrast of the refractive index between the PNC-monolayer and its upper and lower dielectric media. As one can see from Figure 3d, when the point dipole source is exactly at the center the spectral shift is practically zero. However, by moving the location of the point emitter toward the top or down surface of the perovskite layer the frequency shift increases, in such a way that our experimental results would be consistent with the point dipole source located between points different from the center of the perovskite layer (Figure 3b), as shown in Figure 3d. On the contrary, the Purcell factor is not as sensitive as the spectral shift when changing the location of the point dipole source, as observed in Figure 3c. Even like that, the experimental values of Purcell factors for samples with spacers 10, 20, and 50 nm can be accounted for by calculated curves with the dipole located out of center, as occurred for the PL peak redshift. Additionally, in Figures S7 and S8 of the Supporting Information, we have included the spectral and spacer dependences of the Purcell factor, for HMM structures with Ag + LiF layers of 40 + 40 nm (Figure S7) and 25 + 35 nm (Figure S8). In the first case (Ag + LiF layers of 40 + 40 nm or filling factor 50%), we obtain a maximum Purcell factor of 3.5 at around 600 nm (see Figure S7), but around 2.2 at 700 nm, whereas in the second case (Ag + LiF layers of 25 + 35 nm or filling factor 42%) we have achieved a shift of the spectral dependence of the Purcell factor toward the red (see Figure S8), being now its peak value closer to the emission wavelength of the $CsPbI_3$ PNCs. From our calculations, a maximum value of Purcell factor in the range 4.5−5 (depending on the dipole position) is theoretically expected for a spacer layer around 2−3 nm (in agreement with ref 75); experimentally, we are able to deposit a minimum of 10 nm thick layer of PMMA (the spacer) in a controlled way, and hence we would expect values in the range 2.8−3.8 (depending on the dipole position), very close to experimental values (see Figure 3a). Of course, the dispersion in the Purcell factor can be also due to inhomogeneities in the spacer thickness and, to a smaller extent (because of less sensitive), inhomogeneities in the Ag/LiF layers; however, the position (or distance between the dipole and the interface with the HMM surface or air) of the radiant dipole will define the PL redshift.

Figure 4 shows the fabricated structure that has been modeled in 3D COMSOL Multiphysics, frequency domain, RF

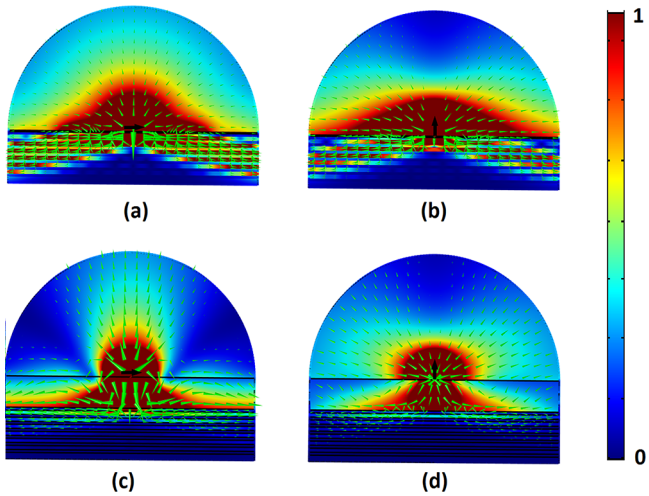

Figure 4. (a, b) Distribution of the normalized electric field $|E|$ of a horizontal and vertical dipole (arrows) located on top of HMM substrate when $d = 10$ nm (c, d) are respectively, correspond to (a, b) when $d = 250$ nm. The point source emits at $\lambda = 705$ nm, and the cones show the direction of the energy flows in logarithmic scale.

module, which is a software based on finite element method (FEM). The oscillating electric point dipole, which emits light at the wavelength of 705 nm, is located on the top surface of the spacer in this simulation. To eliminate the reflection from the outer boundaries, the model is truncated by a perfectly matched layer (PML). This figure illustrates the normalized spatial distribution of the absolute value of the electric field of a point source dipole, with the polarization parallel (Figure 4a−c) and perpendicular (Figure 4b−d) to the multilayer stacks, when it is located at the top surface of the thinnest (Figure 4a−b corresponding to $d = 10$ nm) and thickest (Figure 4c−d corresponding to $d = 250$ nm) spacers of the same HMM structure (25 + 35 nm). To show the propagation of the energy flux, we plotted the Poynting vectors in logarithmic scale within the plane where the dipole oscillates. Additionally, the electric field is spatially expanded into the Ag-LiF metal-dielectric multilayer for both dipole polarizations when the dipole gets close to the HMM structure (by using sufficiently thin spacers). The power dissipated down to the HMM structure is the key physics to understand the observed increase of the spontaneous emission rate of our emitters. On the contrary, for a very thick spacer (the case of our reference device), the point dipole is very far from the multilayer, and its interaction with the metal-dielectric multilayer is substantially reduced, and hence a great amount of the dipole power emits to the top side of the HMM structure.

CONCLUSION

To summarize, we investigated an enhancement of the rate of spontaneous emission of $CsPbI_3$ PNCs by means of HMM substrates. These substrates have been fabricated by the alternative deposition of thin metal (Ag) and dielectric (LiF) layers by means of thermal evaporation. The coupling of excitons photogenerated in $CsPbI_3$ PNCs to the optical modes of these HMM substrates induces a reduction by more than a factor 3 of the exciton radiative lifetime due to the Purcell effect, as measured in the sample with a nominal spacer

https://dx.doi.org/10.1021/acsphotonics.0c01219
ACS Photonics 2020, 7, 3152−3160

thickness (distance between HMM and QEs) of 10 nm. Along with that, varying the spacer (and therefore the exciton-HMM coupling) affects also the PL peak wavelength, which is shifted to the longer wavelengths by up to 8 nm for the thinnest spacer. These experimental results are in agreement with theoretical calculations. These results are important for the future development of single photon sources and other quantum photonic applications based on the combination and integration of perovskite nanocrystals (for which different emission wavelengths are possible) and HMM structures, and eventually nanostructure for further Purcell enhancing.

■ ASSOCIATED CONTENT

Supporting Information

The Supporting Information is available free of charge at https://pubs.acs.org/doi/10.1021/acsphotonics.0c01219.

(1) Details of another HMM structure with 50% filling factor of metal. (2) The delayed luminescence in perovskite nanocrystals and effect on Purcell factor. (3) Additional experimental results in the HMM structure with 42% filling factor of metal. (4) Purcell factor of the HMM structures as a function of wavelength and spacer thickness (PDF)

■ AUTHOR INFORMATION

Corresponding Authors

Juan P. Martínez-Pastor − *Instituto de Ciencia de Materiales (ICMUV), Universidad de Valencia, 46980 Paterna, Spain;* orcid.org/0000-0003-3683-0578; Email: Juan.Mtnez.Pastor@uv.es

Carlos J. Zapata-Rodríguez − *Departament d'Òptica i Optometria i Ciències de la Visió, Facultad de Física, Universitat de València, 46100 Burjassot, Spain;* Email: Carlos.Zapata@uv.es

Authors

Hamid Pashaei Adl − *Instituto de Ciencia de Materiales (ICMUV), Universidad de Valencia, 46980 Paterna, Spain*

Setatira Gorji − *Instituto de Ciencia de Materiales (ICMUV), Universidad de Valencia, 46980 Paterna, Spain*

Mojtaba Karimi Habil − *Faculty of Physics, University of Tabriz, 51664 Tabriz, Iran*

Isaac Suárez − *Instituto de Ciencia de Materiales (ICMUV), Universidad de Valencia, 46980 Paterna, Spain; Departamento de Ingeniería Electrónica, Escuela Técnica Superior de Ingeniería, Universidad de Valencia, 46100 Burjassot, Spain;* orcid.org/0000-0002-2773-8801

Vladimir S. Chirvony − *Instituto de Ciencia de Materiales (ICMUV), Universidad de Valencia, 46980 Paterna, Spain;* orcid.org/0000-0003-4121-9773

Andrés F. Gualdrón-Reyes − *Institute of Advanced Materials (INAM), Universitat Jaume I (UJI), 12071 Castelló de la Plana, Spain;* orcid.org/0000-0002-0208-9235

Iván Mora-Seró − *Institute of Advanced Materials (INAM), Universitat Jaume I (UJI), 12071 Castelló de la Plana, Spain;* orcid.org/0000-0003-2508-0994

Luisa M. Valencia − *Departamento de Ciencia de los Materiales e IM y QI. F. Ciencias, IMEYMAT, Campus Río San Pedro, Universidad de Cádiz, 11510 Puerto Real (Cádiz), Spain*

María de la Mata − *Departamento de Ciencia de los Materiales e IM y QI. F. Ciencias, IMEYMAT, Campus Río San Pedro, Universidad de Cádiz, 11510 Puerto Real (Cádiz), Spain;* orcid.org/0000-0002-1581-4838

Jesús Hernández-Saz − *Departamento de Ingeniería y Ciencia de los Materiales y del Transporte, Escuela Técnica Superior de Ingeniería, Universidad de Sevilla, 41092 Sevilla, Spain;* orcid.org/0000-0002-6630-7203

Sergio I. Molina − *Departamento de Ciencia de los Materiales e IM y QI. F. Ciencias, IMEYMAT, Campus Río San Pedro, Universidad de Cádiz, 11510 Puerto Real (Cádiz), Spain*

Complete contact information is available at: https://pubs.acs.org/10.1021/acsphotonics.0c01219

Notes

The authors declare no competing financial interest.

■ ACKNOWLEDGMENTS

Financial support from Spanish MINECO through Projects No. TEC2017-86102-C2-1-R and TEC2017-86102-C2-2-R, the European Research Council (ERC) via Consolidator Grant (724424-No-LIMIT), the Generalitat Valenciana via Prometeo Grant Q-Devices (Prometeo/2018/098), the 2014-2020 ERDF Operational Programme, and the Junta de Andalucía (FEDER-UCA18-106586 and TEP946 INNANOMAT research group) are gratefully acknowledged. S.G. acknowledges her "Grisolia" grant from Generalitat Valenciana. M.dlM. acknowledges financial support from MICINN (IJCI-2017-31507).

■ REFERENCES

(1) Liu, Y.; Zhang, X. Metamaterials: a new frontier of science and technology. *Chem. Soc. Rev.* **2011**, *40*, 2494−2507.

(2) Smith, D. R.; Pendry, J. B.; Wiltshire, M. C. Metamaterials and negative refractive index. *Science* **2004**, *305*, 788−792.

(3) Shalaev, V. M. Optical negative-index metamaterials. *Nat. Photonics* **2007**, *1*, 41.

(4) Wood, B. Structure and properties of electromagnetic metamaterials. *Laser Photonics Rev.* **2007**, *1*, 249−259.

(5) Poddubny, A.; Iorsh, I.; Belov, P.; Kivshar, Y. Hyperbolic metamaterials. *Nat. Photonics* **2013**, *7*, 948.

(6) Ferrari, L.; Wu, C.; Lepage, D.; Zhang, X.; Liu, Z. Hyperbolic metamaterials and their applications. *Prog. Quantum Electron.* **2015**, *40*, 1−40.

(7) Smalley, J. S.; Vallini, F.; Zhang, X.; Fainman, Y. Dynamically tunable and active hyperbolic metamaterials. *Adv. Opt. Photonics* **2018**, *10*, 354−408.

(8) Yin, X.; Zhu, H.; Guo, H.; Deng, M.; Xu, T.; Gong, Z.; Li, X.; Hang, Z. H.; Wu, C.; Li, H.; et al. Hyperbolic metamaterial devices for wavefront manipulation. *Laser & Photonics Reviews* **2019**, *13*, 1800081.

(9) Maier, S. A. *Plasmonics: Fundamentals and Applications*; Springer Science & Business Media, 2007.

(10) Maier, S. A.; Atwater, H. A. Plasmonics: Localization and guiding of electromagnetic energy in metal/dielectric structures. *J. Appl. Phys.* **2005**, *98*, 011101.

(11) Barnes, W. L.; Dereux, A.; Ebbesen, T. W. Surface plasmon subwavelength optics. *Nature* **2003**, *424*, 824.

(12) Sreekanth, K. V.; Krishna, K. H.; De Luca, A.; Strangi, G. Large spontaneous emission rate enhancement in grating coupled hyperbolic metamaterials. *Sci. Rep.* **2015**, *4*, 6340.

(13) Park, N.-G. Organometal perovskite light absorbers toward a 20% efficiency low-cost solid-state mesoscopic solar cell. *J. Phys. Chem. Lett.* **2013**, *4*, 2423−2429.

(14) Snaith, H. J. Perovskites: the emergence of a new era for low-cost, high-efficiency solar cells. *J. Phys. Chem. Lett.* **2013**, *4*, 3623−3630.

(15) Nie, W.; Tsai, H.; Asadpour, R.; Blancon, J.-C.; Neukirch, A. J.; Gupta, G.; Crochet, J. J.; Chhowalla, M.; Tretiak, S.; Alam, M. A.; et al. High-efficiency solution-processed perovskite solar cells with millimeter-scale grains. *Science* **2015**, *347*, 522−525.
(16) Jeon, N. J.; Noh, J. H.; Yang, W. S.; Kim, Y. C.; Ryu, S.; Seo, J.; Seok, S. I. Compositional engineering of perovskite materials for high-performance solar cells. *Nature* **2015**, *517*, 476−480.
(17) Correa-Baena, J.-P.; Abate, A.; Saliba, M.; Tress, W.; Jacobsson, T. J.; Grätzel, M.; Hagfeldt, A. The rapid evolution of highly efficient perovskite solar cells. *Energy Environ. Sci.* **2017**, *10*, 710−727.
(18) Luo, Q.; Ma, H.; Hou, Q.; Li, Y.; Ren, J.; Dai, X.; Yao, Z.; Zhou, Y.; Xiang, L.; Du, H.; et al. All-carbon-electrode-based endurable flexible perovskite solar cells. *Adv. Funct. Mater.* **2018**, *28*, 1706777.
(19) Shin, S. S.; Suk, J. H.; Kang, B. J.; Yin, W.; Lee, S. J.; Noh, J. H.; Ahn, T. K.; Rotermund, F.; Cho, I. S.; Seok, S. I. Energy-level engineering of the electron transporting layer for improving open-circuit voltage in dye and perovskite-based solar cells. *Energy Environ. Sci.* **2019**, *12*, 958−964.
(20) Protesescu, L.; Yakunin, S.; Bodnarchuk, M. I.; Krieg, F.; Caputo, R.; Hendon, C. H.; Yang, R. X.; Walsh, A.; Kovalenko, M. V. Nanocrystals of cesium lead halide perovskites (CsPbX3, X= Cl, Br, and I): novel optoelectronic materials showing bright emission with wide color gamut. *Nano Lett.* **2015**, *15*, 3692−3696.
(21) Zhang, F.; Zhong, H.; Chen, C.; Wu, X.-g.; Hu, X.; Huang, H.; Han, J.; Zou, B.; Dong, Y. Brightly luminescent and color-tunable colloidal CH3NH3PbX3 (X= Br, I, Cl) quantum dots: potential alternatives for display technology. *ACS Nano* **2015**, *9*, 4533−4542.
(22) Kovalenko, M. V.; Protesescu, L.; Bodnarchuk, M. I. Properties and potential optoelectronic applications of lead halide perovskite nanocrystals. *Science* **2017**, *358*, 745−750.
(23) Li, X.; Cao, F.; Yu, D.; Chen, J.; Sun, Z.; Shen, Y.; Zhu, Y.; Wang, L.; Wei, Y.; Wu, Y.; et al. All inorganic halide perovskites nanosystem: synthesis, structural features, optical properties and optoelectronic applications. *Small* **2017**, *13*, 1603996.
(24) Hassanabadi, E.; Latifi, M.; Gualdron-Reyes, A. F.; Masi, S.; Yoon, S. J.; Poyatos, M.; Julian-Lopez, B.; Mora-Sero, I.; et al. Ligand & Band Gap Engineering: Tailoring the Protocol Synthesis for Achieving High-Quality CsPbI3 Quantum Dots. *Nanoscale* **2020**, *12*, 14194.
(25) Navarro Arenas, J.; Soosaimanickam, A.; Pashaei Adl, H.; Abargues, R.; Boix, P. P.; Rodríguez-Cantó, P. J.; Martínez-Pastor, J. P. Ligand-Length Modification in $CsPbBr_3$ Perovskite Nanocrystals and Bilayers with PbS Quantum Dots for Improved Photodetection Performance. *Nanomaterials* **2020**, *10*, 1297.
(26) Hu, F.; Zhang, H.; Sun, C.; Yin, C.; Lv, B.; Zhang, C.; Yu, W. W.; Wang, X.; Zhang, Y.; Xiao, M. Single Photon Emission from Single Perovskite Nanocrystals of Cesium Lead Bromide. *ACS Nano* **2015**, *9*, 12410.
(27) Utzat, H.; Sun, W.; Kaplan, A. E.; Krieg, F.; Ginterseder, M.; Spokoyny, B.; Klein, N. D.; Shulenberger, K. E.; Perkinson, C. F.; Kovalenko, M. V.; et al. Coherent single-photon emission from colloidal lead halide perovskite quantum dots. *Science* **2019**, *363*, 1068−1072.
(28) Li, C.; Xu, Z.-Q.; Mendelson, N.; Kianinia, M.; Toth, M.; Aharonovich, I. Purification of single-photon emission from hBN using post-processing treatments. *Nanophotonics* **2019**, *8*, 2049−2055.
(29) Turiansky, M.; Alkauskas, A.; Bassett, L.; Van de Walle, C. Boron Dangling Bonds as Single Photon Emitters in Hexagonal Boron Nitride. *Phys. Rev. Lett.* **2019**, DOI: 10.1103/PhysRevLett.123.127401.
(30) Sun, Y.; Yaroshenko, V.; Chebykin, A.; Ageev, E.; Makarov, S.; Zuev, D. Metal-dielectric nanoantenna for radiation control of a single-photon emitter. *Opt. Mater. Express* **2020**, *10*, 29−35.
(31) Shalaginov, M. Y.; Vorobyov, V. V.; Liu, J.; Ferrera, M.; Akimov, A. V.; Lagutchev, A.; Smolyaninov, A. N.; Klimov, V. V.; Irudayaraj, J.; Kildishev, A. V.; et al. Enhancement of single-photon emission from nitrogen-vacancy centers with TiN/(Al, Sc) N hyperbolic metamaterial. *Laser & Photonics Reviews* **2015**, *9*, 120−127.
(32) Vahala, K. J. Optical microcavities. *Nature* **2003**, *424*, 839−846.
(33) Shen, S.; Li, J.; Wu, Y. Magnetically controllable photon blockade under a weak quantum-dot−cavity coupling condition. *Phys. Rev. A: At., Mol., Opt. Phys.* **2020**, *101*, 023805.
(34) Gérard, J.; Sermage, B.; Gayral, B.; Legrand, B.; Costard, E.; Thierry-Mieg, V. Enhanced spontaneous emission by quantum boxes in a monolithic optical microcavity. *Phys. Rev. Lett.* **1998**, *81*, 1110.
(35) Takahashi, H.; Kassa, E.; Christoforou, C.; Keller, M. Strong coupling of a single ion to an optical cavity. *Phys. Rev. Lett.* **2020**, *124*, 013602.
(36) Reithmaier, J. P.; Sek, G.; Loffler, A.; Hofmann, C.; Kuhn, S.; Reitzenstein, S.; Keldysh, L. V.; Kulakovskii, V. D.; Reinecke, T. L.; Forchel, A. Strong coupling in a single quantum dot−semiconductor microcavity system. *Nature* **2004**, *432*, 197−200.
(37) Li, L.; Wang, W.; Luk, T. S.; Yang, X.; Gao, J. Enhanced quantum dot spontaneous emission with multilayer metamaterial nanostructures. *ACS Photonics* **2017**, *4*, 501−508.
(38) Wang, L.; Li, S.; Zhang, B.; Qin, Y.; Tian, Z.; Fang, Y.; Li, Y.; Liu, Z.; Mei, Y. Asymmetrically curved hyperbolic metamaterial structure with gradient thicknesses for enhanced directional spontaneous emission. *ACS Appl. Mater. Interfaces* **2018**, *10*, 7704−7708.
(39) Roth, D. J.; Ginzburg, P.; Hirvonen, L. M.; Levitt, J. A.; Nasir, M. E.; Suhling, K.; Richards, D.; Podolskiy, V. A.; Zayats, A. V. Singlet−Triplet Transition Rate Enhancement inside Hyperbolic Metamaterials. *Laser Photonics Rev.* **2019**, *13*, 1900101.
(40) Lee, K. J.; Lee, Y. U.; Kim, S. J.; André, P. Hyperbolic dispersion dominant regime identified through spontaneous emission variations near metamaterial interfaces. *Adv. Mater. Interfaces* **2018**, *5*, 1701629.
(41) Lu, D.; Ferrari, L.; Kan, J. J.; Fullerton, E. E.; Liu, Z. Optimization of nanopatterned multilayer hyperbolic metamaterials for spontaneous light emission enhancement. *Phys. Status Solidi A* **2018**, *215*, 1800263.
(42) Morozov, K. M.; Ivanov, K. A.; de Sa Pereira, D.; Menelaou, C.; Monkman, A. P.; Pozina, G.; Kaliteevski, M. A. Revising of the Purcell effect in periodic metal-dielectric structures: the role of absorption. *Sci. Rep.* **2019**, *9*, 1−9.
(43) Caligiuri, V.; Palei, M.; Imran, M.; Manna, L.; Krahne, R. Planar double-epsilon-near-zero cavities for spontaneous emission and Purcell effect enhancement. *ACS Photonics* **2018**, *5*, 2287−2294.
(44) Hennessy, K.; Badolato, A.; Winger, M.; Gerace, D.; Atatüre, M.; Gulde, S.; Fält, S.; Hu, E. L.; Imamoğlu, A. Quantum nature of a strongly coupled single quantum dot−cavity system. *Nature* **2007**, *445*, 896−899.
(45) Purcell, E. M.; Torrey, H. C.; Pound, R. V. Resonance absorption by nuclear magnetic moments in a solid. *Phys. Rev.* **1946**, *69*, 37.
(46) Kuhn, H. Classical aspects of energy transfer in molecular systems. *J. Chem. Phys.* **1970**, *53*, 101−108.
(47) Hider, M. H.; Leung, P. Frequency shifts of molecules at rough metal surfaces. *Phys. Rev. B: Condens. Matter Mater. Phys.* **1991**, *44*, 3262.
(48) Morawitz, H. Self-coupling of a two-level system by a mirror. *Phys. Rev.* **1969**, *187*, 1792.
(49) Borensztein, Y.; Abeles, F.; Lopez-Rios, T. Frequency shifts of an ensemble of electric dipole resonances near a conducting surface. *Phys. Rev. Lett.* **1984**, *53*, 854.
(50) Holland, W.; Hall, D. Frequency shifts of an electric-dipole resonance near a conducting surface. *Phys. Rev. Lett.* **1984**, *52*, 1041.
(51) Chance, R.; Prock, A.; Silbey, R. Frequency shifts of an electric-dipole transition near a partially reflecting surface. *Phys. Rev. A: At., Mol., Opt. Phys.* **1975**, *12*, 1448.
(52) Gualdron-Reyes, A. F.; Yoon, S. J.; Barea, E. M.; Agouram, S.; Munoz-Sanjose, V.; Melendez, A. M.; Nino-Gomez, M. E.; Mora-Sero, I. Controlling the phase segregation in mixed halide perovskites through nanocrystal size. *ACS Energy Letters* **2019**, *4*, 54−62.
(53) Saliba, M.; Correa-Baena, J.-P.; Wolff, C. M.; Stolterfoht, M.; Phung, N.; Albrecht, S.; Neher, D.; Abate, A. How to Make over 20%

Efficient Perovskite Solar Cells in Regular (n−i−p) and Inverted (p−i−n) Architectures. *Chem. Mater.* **2018**, *30*, 4193−4201.
(54) Cortes, C.; Newman, W.; Molesky, S.; Jacob, Z. Quantum nanophotonics using hyperbolic metamaterials. *J. Opt.* **2012**, *14*, 063001.
(55) Noginov, M.; Barnakov, Y. A.; Zhu, G.; Tumkur, T.; Li, H.; Narimanov, E. Bulk photonic metamaterial with hyperbolic dispersion. *Appl. Phys. Lett.* **2009**, *94*, 151105.
(56) Mahmoodi, M.; Tavassoli, S. H.; Takayama, O.; Sukham, J.; Malureanu, R.; Lavrinenko, A. V. Existence Conditions of High-k Modes in Finite Hyperbolic Metamaterials. *Laser & Photonics Reviews* **2019**, *13*, 1800253.
(57) Navarro-Arenas, J.; Suárez, I.; Chirvony, V. S.; Gualdrón-Reyes, A. F.; Mora-Seró, I.; Martínez-Pastor, J. Single-Exciton Amplified Spontaneous Emission in Thin Films of CsPbX3 (X= Br, I) Perovskite Nanocrystals. *J. Phys. Chem. Lett.* **2019**, *10*, 6389−6398.
(58) Chirvony, V. S.; Martínez-Pastor, J. P. Trap-Limited Dynamics of Excited Carriers and Interpretation of the Photoluminescence Decay Kinetics in Metal Halide Perovskites. *J. Phys. Chem. Lett.* **2018**, *9*, 4955−4962.
(59) Chirvony, V. S.; Sekerbayev, K. S.; Adl, H. P.; Suárez, I.; Taurbayev, Y. T.; Gualdrón-Reyes, A. F.; Mora-Seró, I.; Martínez-Pastor, J. P. Interpretation of the photoluminescence decay kinetics in metal halide perovskite nanocrystals and thin polycrystalline films. *J. Lumin.* **2020**, *221*, 117092.
(60) Krishnamoorthy, H. N.; Jacob, Z.; Narimanov, E.; Kretzschmar, I.; Menon, V. M. Topological transitions in metamaterials. *Science* **2012**, *336*, 205−209.
(61) Krishna, K. H.; Sreekanth, K.; Strangi, G. Dye-embedded and nanopatterned hyperbolic metamaterials for spontaneous emission rate enhancement. *J. Opt. Soc. Am. B* **2016**, *33*, 1038−1043.
(62) Gontijo, I.; Boroditsky, M.; Yablonovitch, E.; Keller, S.; Mishra, U.; DenBaars, S. Coupling of InGaN quantum-well photoluminescence to silver surface plasmons. *Phys. Rev. B: Condens. Matter Mater. Phys.* **1999**, *60*, 11564.
(63) Zheng, X.; Hou, Y.; Sun, H.-T.; Mohammed, O. F.; Sargent, E. H.; Bakr, O. M. Reducing Defects in Halide Perovskite Nanocrystals for Light-Emitting Applications. *J. Phys. Chem. Lett.* **2019**, *10*, 2629−2640.
(64) Ferrari, L.; Lu, D.; Lepage, D.; Liu, Z. Enhanced spontaneous emission inside hyperbolic metamaterials. *Opt. Express* **2014**, *22*, 4301−4306.
(65) Ford, G. W.; Weber, W. H. Electromagnetic interactions of molecules with metal surfaces. *Phys. Rep.* **1984**, *113*, 195−287.
(66) Diroll, B. T.; Zhou, H.; Schaller, R. D. Low-temperature absorption, photoluminescence, and lifetime of CsPbX3 (X= Cl, Br, I) nanocrystals. *Adv. Funct. Mater.* **2018**, *28*, 1800945.
(67) Sun, L.; Jiang, C. Quantum interference in a single anisotropic quantum dot near hyperbolic metamaterials. *Opt. Express* **2016**, *24*, 7719−7727.
(68) Shalaginov, M. Y.; Ishii, S.; Liu, J.; Liu, J.; Irudayaraj, J.; Lagutchev, A.; Kildishev, A.; Shalaev, V. Broadband enhancement of spontaneous emission from nitrogen-vacancy centers in nanodiamonds by hyperbolic metamaterials. *Appl. Phys. Lett.* **2013**, *102*, 173114.
(69) Tumkur, T.; Zhu, G.; Black, P.; Barnakov, Y. A.; Bonner, C.; Noginov, M. Control of spontaneous emission in a volume of functionalized hyperbolic metamaterial. *Appl. Phys. Lett.* **2011**, *99*, 151115.
(70) Jacob, Z.; Kim, J.-Y.; Naik, G. V.; Boltasseva, A.; Narimanov, E. E.; Shalaev, V. M. Engineering photonic density of states using metamaterials. *Appl. Phys. B: Lasers Opt.* **2010**, *100*, 215−218.
(71) Werner, J.; Nogay, G.; Sahli, F.; Yang, T. C.-J.; Brauninger, M.; Christmann, G.; Walter, A.; Kamino, B. A.; Fiala, P.; Loper, P.; et al. Complex refractive indices of cesium−formamidinium-based mixed-halide perovskites with optical band gaps from 1.5 to 1.8 eV. *ACS Energy Letters* **2018**, *3*, 742−747.
(72) Rakić, A. D.; Djurišić, A. B.; Elazar, J. M.; Majewski, M. L. Optical properties of metallic films for vertical-cavity optoelectronic devices. *Appl. Opt.* **1998**, *37*, 5271−5283.
(73) Aspnes, D. E.; Studna, A. Dielectric functions and optical parameters of si, ge, gap, gaas, gasb, inp, inas, and insb from 1.5 to 6.0 ev. *Phys. Rev. B: Condens. Matter Mater. Phys.* **1983**, *27*, 985.
(74) Novotny, L.; Hecht, B. *Principles of Nano-Optics*; Cambridge University Press, 2012.
(75) Lin, H.-I.; Shen, K.-C.; Liao, Y.-M.; Li, Y.-H.; Perumal, P.; Haider, G.; Cheng, B. H.; Liao, W.-C.; Lin, S.-Y.; Lin, W.-J.; et al. Integration of nanoscale light emitters and hyperbolic metamaterials: an efficient platform for the enhancement of random laser action. *ACS Photonics* **2018**, *5*, 718−727.

https://dx.doi.org/10.1021/acsphotonics.0c01219
ACS Photonics 2020, 7, 3152−3160